

## Article

# A Novel Leak-Proof Thermal Conduction Slot Battery Thermal Management System Coupled with Phase Change Materials and Liquid-Cooling Strategies

Wenjun Zhang <sup>1</sup>, Jianguyun Zhang <sup>1,\*</sup>, Guoqing Zhang <sup>1</sup>, Yanxin Hu <sup>1</sup>, Dan Shao <sup>2,\*</sup>, Liqin Jiang <sup>3</sup> and Yuliang Wen <sup>4</sup>

<sup>1</sup> School of Materials and Energy, Guangdong University of Technology, Guangzhou 510006, China; 2112102258@mail2.gdut.edu.cn (W.Z.); peter008@gdut.edu.cn (G.Z.); huyanxin825@gdut.edu.cn (Y.H.)

<sup>2</sup> Guangdong Key Laboratory of Battery Safety, Guangzhou Institute of Energy Testing, Guangzhou 511447, China

<sup>3</sup> Guangdong Zhuhai Supervision Testing Institute of Quality and Metrology, Zhuhai 519000, China; jerrostony@163.com

<sup>4</sup> Dongguan Guixiang Insulation Material Co., Ltd., Dongguan 523861, China; weny@dggguixiang.com

\* Correspondence: zhangjy008@gdut.edu.cn (J.Z.); shao1005@163.com (D.S.)



**Citation:** Zhang, W.; Zhang, J.; Zhang, G.; Hu, Y.; Shao, D.; Jiang, L.; Wen, Y. A Novel Leak-Proof Thermal Conduction Slot Battery Thermal Management System Coupled with Phase Change Materials and Liquid-Cooling Strategies. *Energies* **2024**, *17*, 939. <https://doi.org/10.3390/en17040939>

Academic Editors: Hamidreza Behi, Danial Karimi, Reza Behi and Masud Behnia

Received: 28 December 2023

Revised: 31 January 2024

Accepted: 3 February 2024

Published: 17 February 2024

**Correction Statement:** This article has been republished with a minor change. The change does not affect the scientific content of the article and further details are available within the backmatter of the website version of this article.



**Copyright:** © 2024 by the authors. Licensee MDPI, Basel, Switzerland. This article is an open access article distributed under the terms and conditions of the Creative Commons Attribution (CC BY) license (<https://creativecommons.org/licenses/by/4.0/>).

**Abstract:** Electric vehicles (EVs) are experiencing explosive developments due to their advantages in energy conservation and environmental protection. As a pivotal component of EVs, the safety performance of lithium-ion batteries directly affects driving miles and even safety; hence, a battery thermal management system (BTMS) is especially important. To improve the thermal safety performance of power battery modules, first, a new leak-proof phase change material (PCM)-coupled liquid-cooled composite BTMS for large-scale battery modules is proposed in this research. Second, the numerical simulation analysis method was utilized to analyze the influences of the fluid flow channel shape, working fluid inlet temperature, inlet velocity, and reverse flow conditions on the BTMS. Eventually, the abovementioned performances were compared with the traditional PCM-coupled liquid-cooling strategy. The relative data indicated that the  $T_{\max}$  was reduced by 17.5% and the  $\Delta T_{\max}$  was decreased by 19.5% compared to the liquid-cooling approach. Further, compared with conventionally designed PCM composite liquid cooling, the  $\Delta T_{\max}$  was reduced by 34.9%. The corresponding data showed that, when using the e-type flow channel, reverse flow II, the inlet flow velocity was 0.001–0.005 m/s, and the inlet temperature was the ambient temperature of the working condition. The thermal performance of the anti-leakage system with a thermal conduction slot PCM-coupled liquid-cooling composite BTMS reached optimal thermal performance. The outcome proved the superiority of the proposed BTMS regarding temperature control and temperature equalization capabilities. It also further reduced the demand for liquid-cooling components, avoided the problem of the easy leakage of the PCM, and decreased energy consumption.

**Keywords:** power lithium-ion batteries; thermal management; phase change materials; liquid cooling; thermal safety

## 1. Introduction

A series of issues, such as energy shortage, environmental pollution, and climate warming, caused by using petroleum or diesel as the main fuel source have gradually become the focus of public attention. Faced with these problems, cleaner, more environmentally friendly, energy-saving, and emission-reducing electric vehicles (EVs) have shown explosive developments [1,2]. As the core components of EVs, lithium-ion power batteries are considered to be a promising power source for new energy vehicles due to their relatively higher energy density and power density [3–5], high discharge voltage platform, and lower self-discharge rates. Nevertheless, lithium-ion power batteries are sensitive to working temperatures. Lithium-ion power batteries generate a high amount of heat

during electrochemical reactions. If there are no reasonable and efficient heat dissipation measures, the excessively high operating temperature after the continuous accumulation of heat will cause the battery performance to decline and the service life to decrease, forming a vicious cycle of “high temperature–high heat–high temperature” [6], followed by combustion, explosions, fire, and other phenomena, and, finally, thermal runaway (TR) problems occur [7,8]. Research indicates that the recommended operating temperature range for lithium-ion power batteries is typically 15–35 °C [9–12], with a suggested temperature difference between batteries of no more than 5 °C [2,13,14]. Thus, employing a battery thermal management system (BTMS) to control a battery within a reasonable temperature range and maintain good temperature uniformity is beneficial to battery life and performance [15,16]. An effective BTMS is necessary for the reliable and safe operation of EVs.

Currently, mainstream battery thermal management systems are mainly enforced according to the heat transfer media, divided into air cooling, liquid cooling, phase change material (PCM) cooling, heat pipe cooling, and hybrid cooling. Air cooling, as a relatively simple and low-cost thermal management system, is suitable for small-scale and low-rate battery modules; however, the low thermal conductivity of air limits its ability to dissipate heat and equalize temperatures in large-scale, high-rate battery modules. As a passive cooling system, PCM cooling has a simple structure and is environmentally friendly. It uses the latent heat of the material itself to control and equalize the temperature; however, the PCM itself has low thermal conductivity, mechanical strength and a slow startup [17], which limit its industrial application. The efficiency of liquid cooling is much higher than that of air cooling and PCM cooling. Furthermore, liquid-cooling systems are usually complicated and bulky [18] and difficult to install and maintain. Additionally, leakage is likely to occur during operation, seriously affecting system safety. As the nominal capacity, energy density, and geometric dimensions of power battery systems continue to increase and upgrade, a single BTMS is far from being able to meet a system’s heat dissipation needs. Hybrid cooling [19] typically combines multiple single cooling methods to enable fully playing to the advantages and disadvantages of multiple cooling methods. It presents a better thermal management performance and is more suitable for the development needs of future EVs. In a hybrid BTMS, coupling-system-based PCMs have attracted widespread attention in recent years. For example, considering the low thermal conductivity of a PCM and the heat accumulation caused by the exhaustion of latent heat, PCMs are combined with active cooling systems or high-thermal-conductivity components [20] to form PCM composite air-cooling BTMSs [21,22], PCM composite liquid-cooling thermal management systems [23–26], and PCM composite heat pipe thermal management systems [27,28]. PCM-coupled liquid cooling combines the advantages of the two heat dissipation strategies. It not only absorbs heat using the high latent heat of a PCM, but it also uses the PCM to fill in the gap between the battery and the cooling system, thus reducing the contact thermal resistance, the battery’s demand for liquid-cooling systems, and the complexity of system design. In addition, the liquid-cooling system can be employed as a cold source for the PCM at this time, thus reducing the temperature of the PCM in time to ensure that the PCM does not overheat and lose its effect.

Liu et al. [23] studied a BTMS coupled with liquid cooling of a paraffin/expanded graphite/high-density ethylene/nano-silver composite PCM. The effects of cold water flow and temperature on the heat dissipation effect of the battery pack were studied at a rate of a 3 C discharge and 1 C charge by changing the connection method of hoses and copper tubes to form the coupling of different PCMs and surface cooling schemes. It was concluded that the heat dissipation effect of the BTMS based on the combination of composite PCM and liquid cooling was much better than that of the heat dissipation system based on a pure PCM, and the former system was more suitable for the cycle charge/discharge of a battery pack. Hekmat et al. [24] proposed a new hybrid BTMS, including PCM and liquid-cooling channels, suitable for achieving perfect uniform temperature distribution in battery modules containing prismatic cells. Numerical simulations were performed to

calculate the performance for different discharge rates and different coolant flow rates. Compared with passive BTMS, the composite BTMS had better temperature uniformity, and the use of a counter flow could enhance the temperature uniformity. Li et al. [29] designed a PCM-coupled liquid-cooling and thermal management system, and they conducted numerical simulations based on the finite volume method, focusing on the terminal layout, coolant flow, different parts of the cooling tube, and location and coupling of the cooling tube factors, such as liquid cooling, and they studied the impact on the operating temperature. The results showed that the appropriate flow and the pipeline layout helped reduce the maximum temperature, and placing the PCM between adjacent cells helped enhance the temperature uniformity of the battery pack. Liu et al. [30] proposed a hybrid cooling system coupling PCM/copper foam with spiral liquid channels for a BTMS. The results indicated that the hybrid system could reduce battery temperature by more than 30 K compared with passive BTMS. Zhang et al. [31] suggested a hybrid cooling system using PCM and liquid cooling to prevent thermal runaway propagation in lithium-ion power battery modules. The findings demonstrated that this combined system effectively integrated the benefits of PCM and liquid thermal management solutions, adequately meeting the cooling requirements under extreme operating conditions. Cao et al. [32] proposed that a low-temperature coolant would increase the temperature difference of a battery pack and reduce the discharge capacity. Thus, if the battery temperature was within the limit, it was preferable to utilize a coolant temperature that was close to the environment. Further, a delayed liquid-cooling strategy was proposed. When the battery was still in a state where the PCM could absorb latent heat, the liquid-cooling system was not activated. The liquid-cooling system was activated again after the battery temperature exceeded a certain range. The results showed that delayed cooling improved the temperature uniformity at high discharge rates, and the composite BTMS could keep the maximum system temperature below 55 °C and the maximum temperature difference below 5 °C at a 4 C discharge rate. Liu et al. [33] proposed a novel hybrid liquid PCM BTMS with a honeycomb structure to solve the temperature rise and temperature difference problems of lithium-ion soft pack battery modules. The results claimed that hybrid cooling could effectively control the maximum temperature of the battery, and the honeycomb fin structure contributed to a greater heat exchange area, increasing the heat exchange power and efficiency. Xiao et al. [34] incorporated expanded graphite (EG) into paraffin to create composite PCM and integrated aluminum fins with liquid cooling to improve heat transfer in order to enhance the performance of PCM-based BTMS. They established and experimentally validated a thermal model for lithium-ion batteries. The outcomes illustrated that the new BTMS notably ameliorated the secondary heat storage issue of PCM and enhanced the temperature uniformity of lithium-ion batteries. The combination of a fin structure and liquid cooling effectively boosted the heat transfer of the composite PCM. Javani et al. [35] conducted an exergy analysis of a coupled liquid-cooling and PCM-cooling system. They found that increasing the PCM mass fraction from 65% to 80% led to improvements in both the coefficient of performance and exergy efficiency, with values rising from 2.78 to 2.85 and from 19.9% to 21%, respectively. However, they also noted that while increasing the PCM mass fraction reduced the overall power consumption of the system, this benefit was counteracted by the increased manufacturing costs and system weight, ultimately resulting in a higher overall power consumption during operation. As a result, Javani et al. proposed a conflicting scenario where different heat sink configurations would require tailored optimization strategies to achieve their most effective performance. Zhao et al. [36] compared the performance of copper-foam-based and EG-based composite phase change materials (CPCMs) in a coupled system. The results showed that the EG-based CPCM outperformed the copper-foam-based CPCM, achieving lower maximum cell temperatures and temperature differences. At a flow rate of 0.001 m/s, the temperature difference among individual cells for the copper-foam-based CPCM was 19 °C, while the EG-based counterpart maintained this difference within 5 K. Zhang et al. [37] introduced a new battery thermal management system (BTMS) that integrated a non-uniform thermal conductivity medium, comprising a

high-thermal-conductivity PCM (a mixture of EG and PA) with a low-thermal-conductivity material. The high-thermal-conductivity PCM was designed to quickly absorb battery-generated heat and effectively conduct it to the liquid-cooling system, thereby reducing the battery temperature. However, the low-thermal-conductivity PCM was intended to absorb heat and impede the transfer of heat between adjacent cells, thus slowing down thermal runaway propagation. This design goal was to mitigate thermal runaway hazards by allowing additional time for intervention and rescue procedures. Ouyang et al. [38] combined PCM, liquid cooling, and insulation materials to address battery thermal management. They surrounded a battery with CPCM and utilized an aerogel frame to isolate individual cells, along with liquid-cooling channels for heat dissipation. Despite significantly delaying thermal runaway propagation, complete eradication was not achieved. In addition, the insulating effect of the aerogel caused heat accumulation in the PCM, requiring timely dissipation and an increased coolant flow rate and thereby impacting thermal performance. Chen et al. [39] studied the distribution of CPCM with varying EG levels in the direction of liquid flow to investigate the impact of different layout lengths on heat dissipation. They divided the system into three sections with lengths of 110 mm, 120 mm, and 130 mm, thus successfully restricting the cell's maximum temperature and maximum temperature difference to 46.35 °C and 3 °C. Zhang et al. [40] developed a coupled battery thermal management system (BTMS) that integrated PCM and liquid cooling, leveraging the high axial thermal conductivity of the cells. Their investigation focused on the effects of the cell-to-cell distance, cell-to-liquid-cooling-channel distance, flow direction, and inlet mass flow rate on the overall cooling performance of the battery pack. The results demonstrated that larger cell spacing allowed for increased PCM accommodation, leading to enhanced thermal storage capacity and cooling efficiency. Lebrouhi et al. [41] investigated the factors affecting the integration of liquid cooling with PCM for BTMS, expanding their analysis to include the coolant inlet temperature and the number of cooling pipes, in addition to the factors mentioned earlier. Tests conducted using coolant inlet temperatures of 10 °C, 15 °C, and 25 °C revealed a significant trend: decreasing the coolant inlet temperature resulted in substantial reductions in the cell temperatures. Specifically, the reduction from a 25 °C to a 10 °C coolant inlet temperature corresponded to a decrease in the maximum battery temperature from 31 °C to 20 °C. An et al. [42] introduced a novel chocolate plate hybrid BTMS integrating a metal lattice PCM liquid-cooled plate. A comparative analysis of a pure liquid-cooled metal plate, a metal plate PCM liquid-cooled plate, and a metal lattice PCM liquid-cooled plate showed that both the metal liquid-cooled and metal lattice PCM liquid-cooled plates exhibited superior performance compared to the pure liquid-cooled plate, with minimal distinctions between the two former options. Hu et al. [43] found that initiating the pump when the cell temperature exceeded the phase change range of the PCM proved to be the optimal approach. This strategy, which involved starting the pump at a lower temperature, effectively mitigated sudden temperature spikes and prevented unnecessary energy wastage by avoiding activation at excessively low temperatures. Conventional experiments and simulations typically determine pump activation timing based on measurements of the battery surface temperatures or those in close proximity to the battery. Hou et al. [44] introduced a model that employed the extended Kalman filter (EKF) for a real-time estimate of battery temperature without requiring additional temperature sensors, demonstrating high accuracy. They confirmed through testing the consistency between actual battery temperature and predicted results across different discharge rates, coolant flow rates, and PCM thicknesses, with a maximum deviation of less than 5%.

According to the above reference review, it could be seen that most of the research on PCM-coupled liquid-cooling composite BTMS has focused on the design of the liquid-cooling plate flow channel structure, the modification or enhancement of PCM, the selection of the coolant, and the direction of export conditions. Although the above research directions had a significant effect on enhancing the hybrid BTMS, they only focused on enhancing the unilateral structure of the composite thermal management system rather than enhancing the entire composite system. In addition, the BTMS with PCM-coupled

with liquid cooling still had problems faced by both PCM cooling and liquid cooling, such as a large volume, a bulky system, leakage of liquid or PCM, and latent heat exhaustion of the PCM as well as other problems. Hybrid thermal management systems with a PCM coupled with liquid cooling would be further enhanced by treating multiple parts of the hybrid thermal management system as a unified whole for structural design or enhancement.

A PCM indirect contact liquid-cooling plate for cylindrical batteries was first designed in this research to solve the aforementioned problems. The designed liquid-cooling plate and PCM were integrated into an integrated structure design, which could not only improve the cooling performance and reduce the weight but also provide a closed package for the PCM to prevent leakage and yield better structural support. A three-channel flow channel was designed in the liquid-cooling plate that could be used to better adjust the flow condition to match the different working conditions of the battery. Additionally, the liquid-cooling plate was designed with a slot matching the cylindrical battery that could be used to better secure the battery, provide a larger heat exchange area, and reduce contact thermal resistance compared to traditional liquid-cooling plates. Compared with the traditional PCM-coupled liquid cooling, the coupling degree of PCM and liquid cooling in the system was higher. When the PCM was placed in the liquid-cooling plate, due to the design of the above battery slot, there were many small compartments inside the liquid-cooling plate. At this time, the wall of the cubicle could act as a fin in contact with the PCM, which greatly enhanced the coupling between the liquid-cooling system and the PCM. This could better combine the advantages of liquid cooling and PCM cooling. Finally, the three-dimensional CFD model was employed to study the cooling effect of the liquid-cooling plate in three different working conditions. Compared with the traditional liquid-cooling plate and the traditional PCM-coupled liquid cooling, the flow conditions, flow channel structure design, and counter fluid were further studied. This research will provide cooling strategy guidance and calculation support for improving the thermal safety performance of large-scale, high-energy-density battery modules and battery packs.

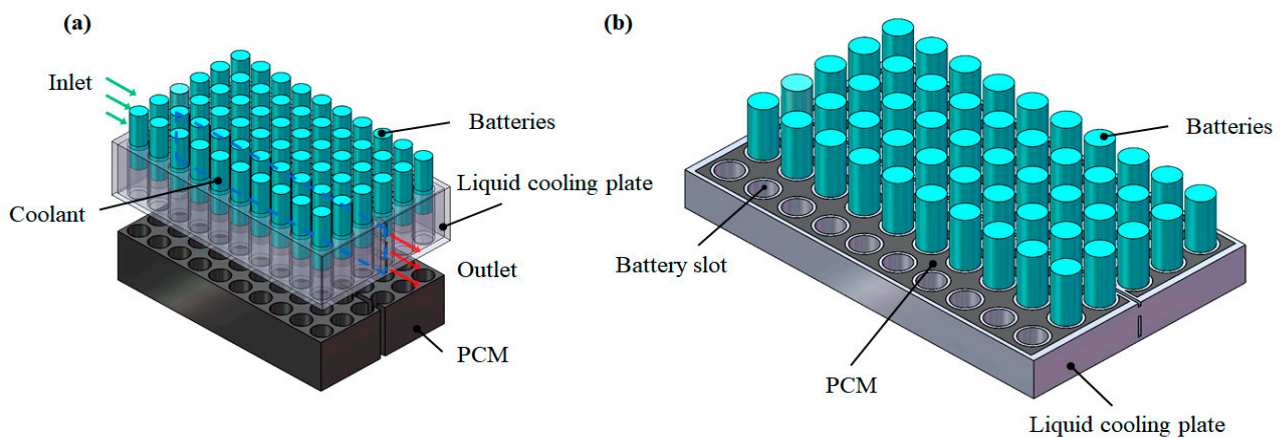
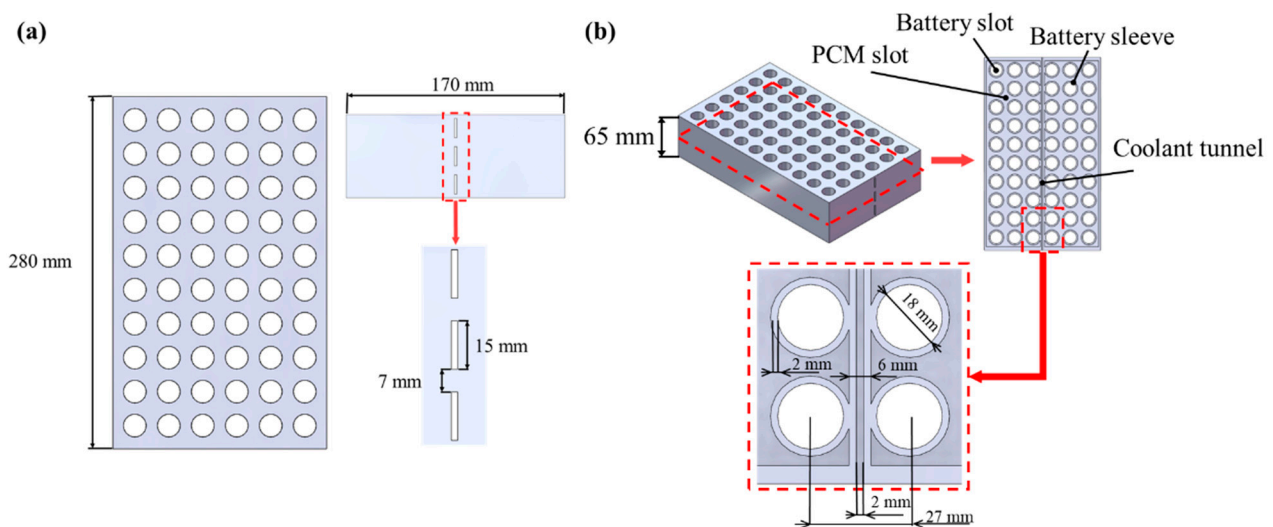
## 2. Model and Methodology

### 2.1. Geometric Model

The battery used in this research was a 18650-type cylindrical battery,  $\text{Li}(\text{Ni}_{0.8}\text{Co}_{0.1}\text{Mn}_{0.1})\text{O}_2/\text{C}$  (NCM811) (Zhengzhou BAK BATTERY Co., Ltd., Zhengzhou, China). The technical specifications of the battery are shown in Table 1. The battery module contained 60 cells. The batteries discussed in the experimental verification section below had the same specifications. The BTMS designed in this research is shown in Figure 1. As can be seen from Figure 1, the aforementioned BTMS mainly consisted of the battery module, the liquid-cooling plate, and the PCM inside the liquid-cooling plate. The external dimensions of the cooling plate were  $280 \times 170 \times 65 \text{ mm}^3$ . The cooling plate was equipped with slots corresponding to the size of the battery, which were designed to fix and fit batteries. The liquid-cooling plate was hollow inside and had a fluid channel with the coolant inlets and outlets on both sides of the cooling plate. The internal design of the composite cooling plate is shown in Figure 2. It can be observed from the figure that the interior of the cooling plate was hollow and divided into multiple zones by slots and fluid channels. In this model, the liquid-cooling plate was made of aluminum, and the natural convection coefficient of the battery surface was  $5 \text{ W}\cdot\text{m}^{-2}\cdot\text{K}^{-1}$  when employing water as a coolant. ANSYS FLUENT software, Ansys 2021 R1 was employed to perform numerical calculations for this model. The materials and physical property parameters are shown in Table 2.

**Table 1.** Parameters of the cylinder cell.

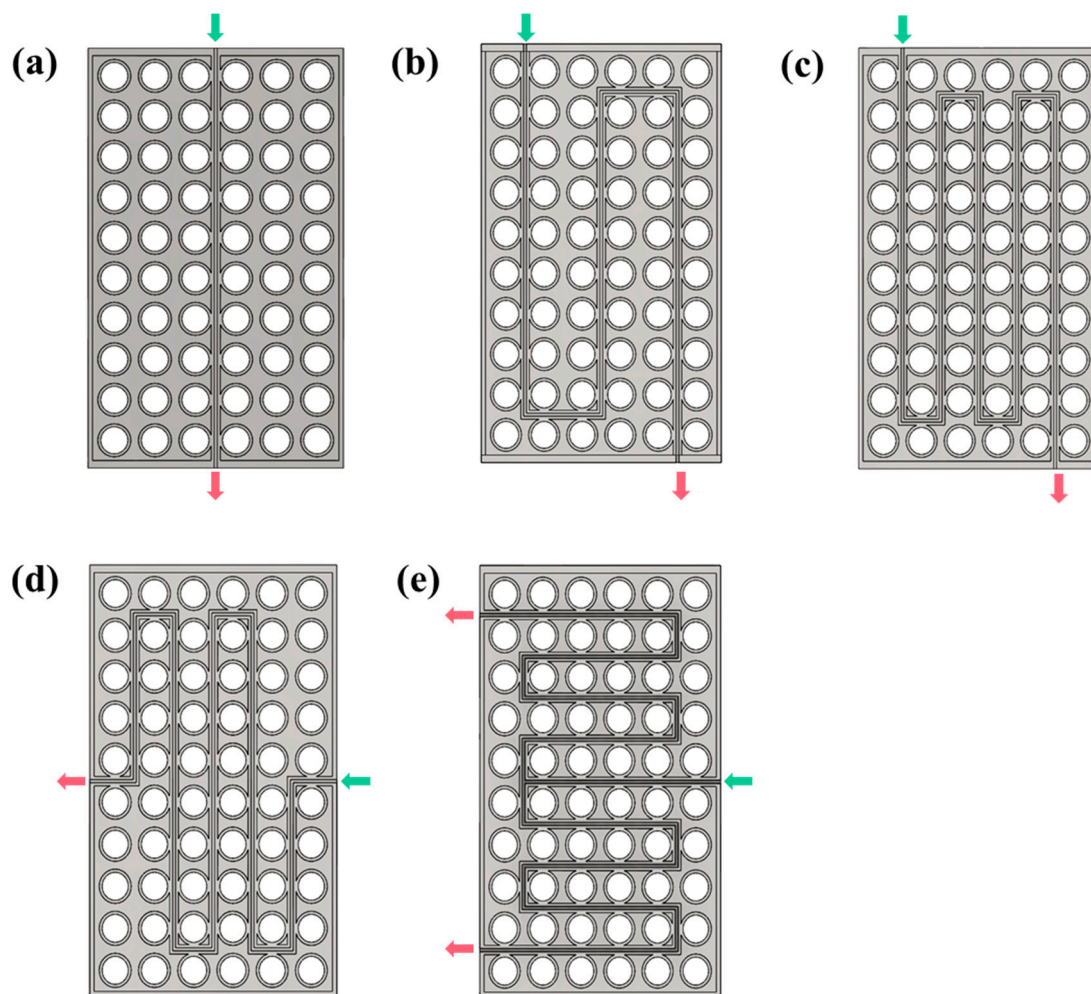
Parameter	Value
Cathode	$\text{Li}(\text{Ni}_{0.8}\text{Co}_{0.1}\text{Mn}_{0.1})\text{O}_2$
Anode	Graphite
Nominal capacity (mAh)	3050
Nominal voltage (V)	3.6
Charge cut-off voltage (V)	4.20
Discharge cut-off voltage (V)	2.5
Energy density (Wh/Kg)	234
Battery dimension (mm)	Height: $64.85 \pm 0.25$ , Diameter: $18.35 \pm 0.15$
Mass (g)	47
Charge temperature range ( $^{\circ}\text{C}$ )	0–45
Discharge temperature range ( $^{\circ}\text{C}$ )	−20–60

**Figure 1.** (a) Schematic diagram of a battery pack with composite liquid-cooling plate (CLCP). (b) Sectional view of the plate.**Figure 2.** Detailed description of the aforementioned BTMS: (a) Top view of the device and details of the entrance. (b) Sectional view of the device.

**Table 2.** Thermo-physical properties of the materials used in this work.

Parameter (Unit)	Battery	PCM	Aluminum Plate	Cooling Water
Thermal conductivity ( $W \cdot m^{-1} \cdot K^{-1}$ )	1.8 (X,Y), 25.6 (Z)	1	202.4	0.6
Specific heat ( $J \cdot kg^{-1} \cdot K^{-1}$ )	1100	2460	871	4182
Density ( $kg \cdot m^{-3}$ )	2481.59	770	2719	998.2
Melting temperature ( $T_S - T_L$ ) ( $^{\circ}C$ )	-	35–37	-	-
Latent heat ( $kJ \cdot kg^{-1}$ )	-	247.6	-	-

Based on the above model, four additional flow channel shapes were designed to improve the performance of the thermal management system by studying the paths and methods of liquid flow in the BTMS. As shown in Figure 3, the additional four flow channel shapes were all snake-like shapes and could be divided into two categories according to the long and short sides of the flow channel entrance and exit, that is, flow from the head and tail of the battery module or flow from the waist. An additional flow inlet and an outlet were designed to achieve counterflow conditions. The detailed heat transfer approaches of the proposed BTMS are illustrated in Figure 4.

**Figure 3.** Concrete design of channel configurations: (a) a-type flow channel, (b) b-type flow channel, (c) c-type flow channel, (d) d-type flow channel, and (e) e-type flow channel.

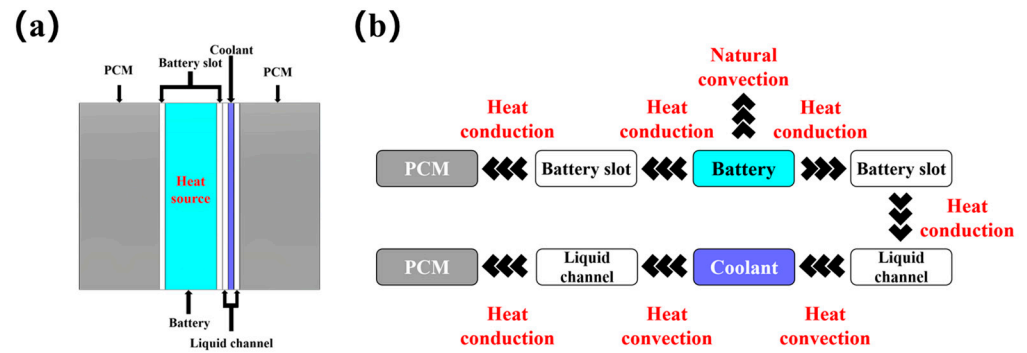


**Figure 4.** (a) Heat transfer route cross-section diagram, and (b) heat transfer roadmap.

## 2.2. Mathematical Model

### 2.2.1. Battery Thermal Model

The thermal model of the battery was employed to simulate its thermal performance and forecast the thermal distribution within the battery module. The temperature distribution of the battery during the charge and discharge process was influenced by its actual heating behavior. As a result, the total heat generated by the battery ( $Q_{gen}$ ) encompassed the following three aspects [45]:

$$Q_{gen} = Q_r + Q_p + Q_j, \quad (1)$$

where  $Q_r$ ,  $Q_p$ , and  $Q_j$  represent reaction heat, polarization heat, and joule heat, respectively. They could be calculated using the following equations, Equations (2)–(4):

$$Q_r = -T_b \Delta S \frac{I}{nF}, \quad (2)$$

where  $T_b$  is the temperature of the battery,  $I$  represents the charge and discharge current,  $n$  represents the number of charges associated with the reaction (for LIB,  $n = 1$ ), and  $F$  is Faraday's constant.

$$Q_p = I^2 R_p = I^2 (R_t - R_e), \quad (3)$$

where  $R_p$ ,  $R_e$ , and  $R_t$  represent the polarization resistance, battery internal resistance, and total resistance, respectively.

$$Q_j = I^2 R_e, \quad (4)$$

where  $I$  is the current of the electrode.

Based on a prior study, the D. Bernardi heat generation model [46] was utilized to examine the heat generation behavior and compute the battery's temperature variation, as shown below:

$$\dot{q} = \frac{I}{V} (E_{oc}) - U - T \frac{dE_{oc}}{dT}, \quad (5)$$

where  $\dot{q}$  is the heat generation of the battery,  $I$  is the charging and discharging current,  $V$  is the volume of the battery,  $E_{OC}$  is the balance electromotive force of the battery,  $U$  is the operating potential of the battery, and  $T$  is the operating temperature of the battery.

Through experiments, the temperature data for the battery discharged at a 2 C rate at three ambient temperatures of 25 °C/35 °C/45 °C were recorded. Figure 5a is a schematic diagram of the experimental device. The battery was placed in a thermostat (ZH-TH-100D, Dongguan Zhenghang Instrument Equipment Co., Ltd., Dongguan, China), and a constant temperature condition was set. The battery was charged and discharged through the battery cabinet (CT-40001-60 V-100 A-NA, Shenzhen Newwell Electronics Co., Ltd., Shenzhen, China) to perform 0.5 C charge and 2 C discharge tests on the battery. There were three T-type thermocouples (TC-TFF 2 × 0.25 × 1000 mm, accuracy ±0.1 °C, USA) distributed on the upper, middle, and lower parts of the battery surface. The thermocouples were connected to the temperature monitoring instrument Agilent (34970 A, Agilent

Technologies, Inc., Loveland, CO, USA) and the data were recorded. The specific test process was to let the battery stand in a constant temperature thermostat for 1 h. Then, after the battery was charged to 4.2 V at a constant current of 0.5 C (1525 mA), the battery was charged at a constant voltage of 4.2 V until the current was less than or equal to 0.01 C (30.5 mA). After the battery stood for 1 h, the battery was discharged at a constant current of 2 C (6100 mA) until it reached a 2.5 V cut-off voltage. The above process was repeated three times and the average temperature data were taken. Based on the experimental data and the battery heat generation model, the battery thermal model was simulated and restored by considering natural convection. As shown in Figure 5b, for the ambient temperatures of 25 °C/35 °C/45 °C, the maximum relative error of the temperature data at a 2 C discharge rate was within ±2%. The data relative error was small, indicating that the simulation model was reliable.

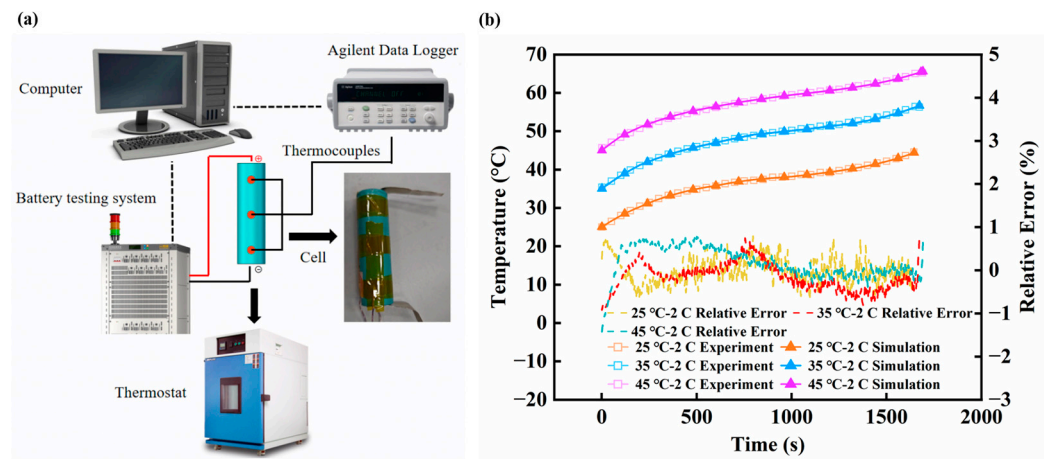


**Figure 5.** (a) Schematic diagram of experimental device, and (b) comparison of experimental and simulation results.

### 2.2.2. Governing Equations

For the coolants, the Reynolds number  $Re$  described the liquid coolant flowing through the flow channel, and was defined as follows:

$$Re = \frac{\rho_c v_c d_c}{\mu_c}, \quad (6)$$

$$d_c = \frac{4A_c}{P_c} = \frac{4\pi r_c^2}{2\pi r_c}, \quad (7)$$

where  $\rho_c$  is the density of the coolant,  $v_c$  is the velocity,  $d_c$  is the hydraulic diameter of the channel,  $A_c$  is the cross-sectional area of the flow channel,  $P_c$  is the wetted perimeter of the flow channel, and  $r_c$  is the radius of the flow channel.

The heat generated during the battery discharge process was transferred to the PCM through the liquid-cooling plate and absorbed by the PCM as latent heat storage. The coolant in the flow channel could take away the heat of the battery and PCM at the same time and recover the latent heat of the PCM. Based on prior work [47], the specific control equations are described as follows:

For lithium-ion power batteries, the energy conservation equation could be written as

$$\rho_b c_{p,b} \frac{\partial T_b}{\partial t} = \nabla(k_b \nabla T_b) + Q_{gen}, \quad (8)$$

where  $\rho_b$ ,  $k_b$ , and  $T_b$  are the density, thermal conductivity, and temperature of the battery, respectively.  $Q_{gen}$  is the calorific value of the battery.

The heat transfer within the *PCM* was controlled by the following equation:

$$\rho_{PCM} \frac{\partial H_{PCM}}{\partial t} = \nabla(k_{PCM} \nabla T_{PCM}), \quad (9)$$

$$H_{PCM} = \int_{T_0}^{T_{PCM}} c_{PCM} dT + \beta L, \quad (10)$$

where  $\rho_{PCM}$ ,  $H_{PCM}$ , and  $k_{PCM}$  are the density, enthalpy, and effective thermal conductivity, respectively, of the *PCM*,  $T_{PCM}$ , and  $T_0$ , with  $T_{PCM}$  and  $T_0$  representing the *PCM* and ambient temperatures.  $L$  is the latent heat of the *PCM*.  $\beta$  is the liquid fraction of the *PCM* and can be expressed as

$$\beta = \begin{cases} 0 & T_{PCM} < T_s \\ \frac{T_{PCM} - T_s}{T_L - T_s} & T_s \leq T_{PCM} < T_L \\ 1 & T_{PCM} > T_L \end{cases}, \quad (11)$$

where  $T_s$  and  $T_L$  are the solid phase and liquid phase temperatures of the *PCM*, respectively.

For the coolants, the conservation equations for continuity, momentum, and energy terms were

$$\frac{\partial \rho_c}{\partial t} + \nabla(\rho_c \vec{v}_c) = 0, \quad (12)$$

$$\rho_c \frac{\partial \vec{v}_c}{\partial t} + \rho_c (\vec{v}_c \nabla) \vec{v}_c = -\nabla P + \nabla(\mu_c \nabla \vec{v}_c), \quad (13)$$

$$\rho_c C_{p,c} \frac{\partial T_c}{\partial t} + \nabla(\rho_c C_{p,c} \vec{v}_c T_c) = \nabla(k_c \nabla T_c). \quad (14)$$

For the flow channel, the energy conservation equation could be expressed as follows:

$$\rho_c C_{p,t} \frac{\partial T_t}{\partial t} = \nabla(k_t \nabla T_t), \quad (15)$$

where  $(\rho_c, \rho_t)$ ,  $(C_{p,c}, C_{p,t})$ ,  $(k_c, k_t)$ , and  $(T_c, T_t)$  are the density, specific heat capacity, thermal conductivity, and temperature of the coolant and the flow channel, respectively.  $\vec{v}_c$ ,  $P$ , and  $\mu_c$  represent the coolant velocity vector, static pressure, and dynamic viscosity, respectively.

During the simulation, the initial state was specified as follows:

$$t = 0,$$

$$T(x, y, z) = T_{amb},$$

where  $T_{amb}$  is the ambient temperature.

The boundary conditions between the battery and the liquid-cooling plate were defined as follows:

$$-k_b \frac{\partial T}{\partial n} = -k_{plate} \frac{\partial T}{\partial n}, \quad (16)$$

where  $k_b$  and  $k_{plate}$  are the thermal conductivities of the battery and liquid-cooling plate, and  $\frac{\partial T}{\partial n}$  represents the temperature gradient.

The boundary conditions for the interface between the flow channel and the coolant were defined as follows:

$$-k_{tube} \frac{\partial T}{\partial n} = -k_c \frac{\partial T}{\partial n} + h_c (T_c - T_{tube}), \quad (17)$$

where  $k_c$  is the thermal conductivity of the coolant,  $h_c$  is the heat transfer coefficient of the liquid coolant, and  $T_{tube}$  is the surface temperature of the internal channel.

The boundary conditions between the liquid-cooling plate and the *PCM* were defined as follows:

$$-k_{plate} \frac{\partial T}{\partial n} = -k_{PCM} \frac{\partial T}{\partial n}, \quad (18)$$

where  $k_{plate}$  and  $k_{PCM}$  are the thermal conductivity of the liquid-cooling plate and the PCM, and  $\frac{\partial T}{\partial n}$  represents the temperature gradient.

The boundary conditions between the battery and the environment were defined as follows:

$$-k_b \frac{\partial T}{\partial n} = h(T_b - T_{amb}), \quad (19)$$

where  $k_b$  represents the thermal conductivity of the battery,  $T_b$  represents the battery temperature, and  $h$  represents the natural convection heat transfer coefficient.

### 2.3. Boundary Conditions and Grid Independence Test

Based on the geometry of the flow channel and the selected flow rate, a laminar flow model ( $Re < 2300$ ) was chosen for the fluid. The simulation calculation adopted the three-dimensional transient Navier–Stokes equation, laminar flow model, and solidification and melting model, and the calculation accuracy was improved by adding control equations. The second-order upwind difference scheme was conducted for fluid kinematics, and the SIMPLE method was used for iterative calculations.

The inlet boundary condition was the velocity inlet, whose value was constant. The outlet boundary condition was a pressure outlet, and the impact of backflow on the main calculation domain was avoided by suppressing the backflow and extending the outlet domain. The natural convection heat transfer between the battery surface and the environment was considered, and the convection heat transfer coefficient was  $5 \text{ W} \cdot \text{m}^{-2} \cdot \text{K}^{-1}$ . The coolant was water, which was considered an incompressible fluid in the calculations. All of the contact surfaces between solids and liquids were set up as fluid-structure coupling. It was assumed that the battery was discharged at a rate of 2 C with a 100% depth of discharge (DOD). Numerical simulations were performed using the battery as a heat source item.

In addition, to better match the model and simplify calculations, the following assumptions were made based on previous work [48–50]:

1. All of the parameters of the battery were constant and isotropic except thermal conductivity.
2. It was assumed that the PCMs used in the model were homogeneous and the properties of the liquid and solid phases were constant and identical. During the phase change, the motion and volume change in PCM were ignored.
3. The liquid-cooling plate was made of aluminum and assumed to be homogeneous, and all parameters were constant and isotropic.
4. It was assumed that the materials were in close contact, and the contact thermal resistance was ignored.
5. There was no slip between the wall and adjacent fluid particles.

For the model calculation accuracy and efficiency, the grid independence was tested. Meshing was performed with Fluent Meshing, poly-hexcore was selected, and inflation was used. As shown in Figure 6a, the mesh was generated densely and uniformly, and the meshes between different materials were transitionally processed. The grid independence test was conducted on the grid numbers from 535,434 to 5,843,719, as shown in Figure 6b. Except for the calculation error for the grid numbers of 535,434, which caused the calculation to be incomplete, all of the other grid numbers were calculated completely. The average temperature of the battery tended to be stable when the number of grids exceeded 1,000,000. The average liquid fraction of the PCM showed a fluctuating trend as the number of grids increased at the beginning and then became stable after the number of grids was 4,000,000. Therefore, this model used a grid number of 4,000,000 levels for calculation.

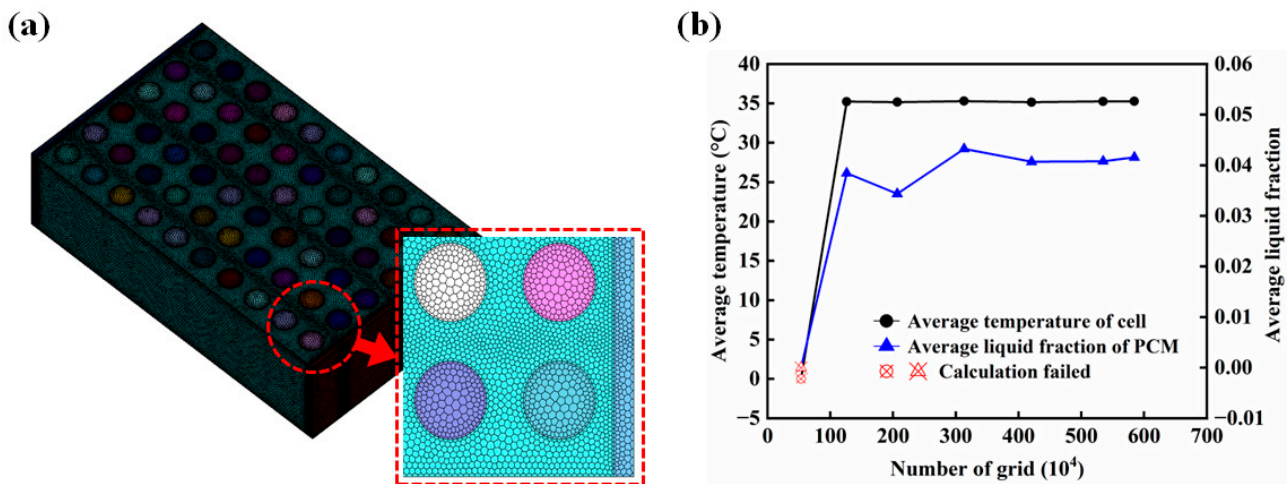


Figure 6. (a) Meshing, and (b) mesh independence analysis.

### 3. Results and Discussion

#### 3.1. Thermal Characterization of CLCP

The battery pack was simulated in three cooling modes, namely, liquid cooling, traditional PCM-coupled liquid cooling, and the new PCM-coupled liquid cooling designed in this research, to verify the impact of the composite liquid-cooling plate on the heat performance. The schematic diagram of liquid cooling and traditional PCM-coupled liquid cooling is shown in Figure 7. The above three cooling systems had the same volume, and the cooling system designed in this research had a weight reduction of 50.2% compared with the traditional liquid-cooling system. By simulating the entire process of the battery at ambient temperatures of 25 °C/35 °C/45 °C, the coolant flow rate was set as 0.005 m/s, the inlet temperature set as 25 °C, and a 2 C discharge cycle (1800 s) were used to explore the function of the CLCP.

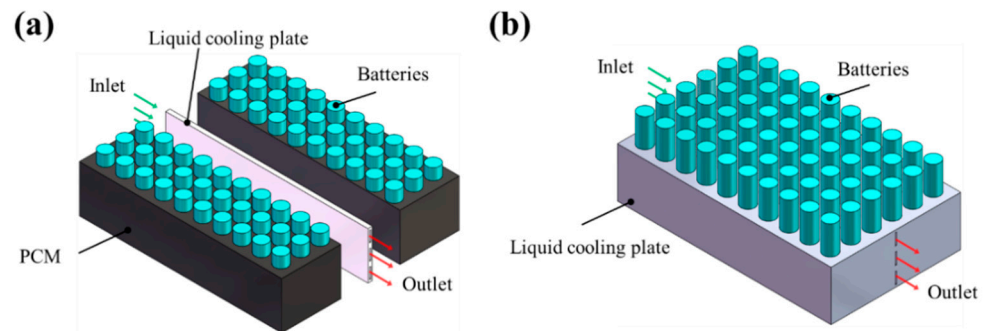
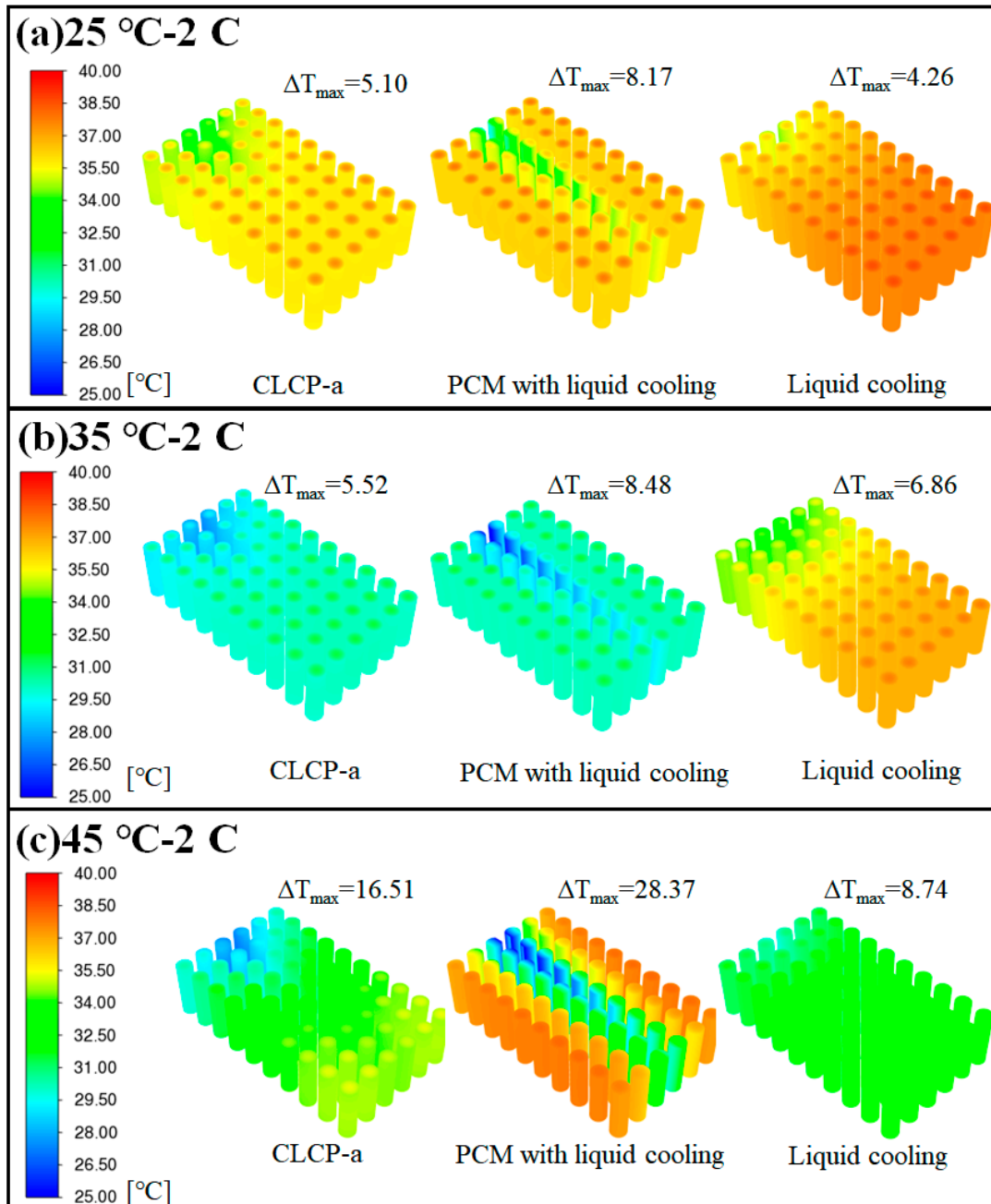


Figure 7. (a) Traditional PCM-coupled liquid cooling and (b) liquid-cooling model.

Figure 8 shows the temperature distribution diagram of the battery at the end of the 2 C discharge (at 1800 s) in the three thermal management modes at 25 °C/35 °C/45 °C ambient temperatures. Through the analysis and comparison, as shown in Figure 8a,b, when the ambient temperature was 25 °C/35 °C, both battery modules that used the PCM for cooling had a lower  $T_{max}$  than the battery modules that used liquid cooling, and the  $T_{max}$  of CLCP-a was lower than or close to that of the other battery modules. When the ambient temperature was 45 °C, as shown in Figure 8c, the PCM lost its function due to the low thermal conductivity of the PCM, which hindered the heat transfer of the battery module. Therefore, the battery module that used liquid cooling for BTMS had the lowest  $T_{max}$ . However, CLCP-a had an aluminum shell similar to liquid-cooling BTMS, so it could have lower  $T_{max}$  than the battery modules that used traditional PCM-coupled with liquid cooling. Notably, CLCP-a could effectively control the temperature of the battery module

before the PCM failed and ensure that the  $T_{\max}$  of the battery module was better than that of the other battery modules after the PCM failed.



**Figure 8.** Temperature distribution diagrams of three types of thermal management systems after discharge (t = 1800 s) for (a) 25 °C-2 C, (b) 35 °C-2 C, and (c) 45 °C-2 C.

The  $\Delta T_{\max}$  of the battery module only changed slightly before the PCM failed. It was believed that the addition of PCM could provide a buffer effect for the battery module to work under extreme working conditions and avoid temperature differences increasing due to operating condition changes. In other words,  $\Delta T_{\max}$  at this time mainly depended on the design of the BTMS, such as the shape of the flow channel, the inlet and outlet flow rates, etc. When the ambient temperature was too high and the PCM failed,  $\Delta T_{\max}$  rose sharply, especially for battery modules that used the liquid-cooling coupled PCM. This was because of the huge difference in the thermal conductivity between the aluminum plate and the

PCM, which could very easily cause a huge temperature gradient. Despite this, CLCP-a could still achieve better temperature uniformity than the traditional PCM coupled with liquid cooling.

To further analyze the effect of CLCP-a, the curve chart of the  $T_{\max}$  change in each battery module for the 2 C discharge cycle at 25 °C/35 °C/45 °C ambient temperature was extracted, as shown in Figure 9. It can be seen from Figure 9a,b that when the  $T_{\max}$  of the battery module was close to 37 °C, there was a significant difference in the  $T_{\max}$  change trend of the battery module using the PCM and the battery module without the PCM, and the BTMS with the PCM slowed down the rate of the temperature rise. Additionally, due to the effect of the PCM, the battery module at the two ambient temperatures of 25 °C/35 °C had a close  $T_{\max}$  after discharging at 2 C. The above situation showed that part of the heat of the battery was absorbed by the PCM, which slowed down the temperature rise of the battery module to a certain extent.

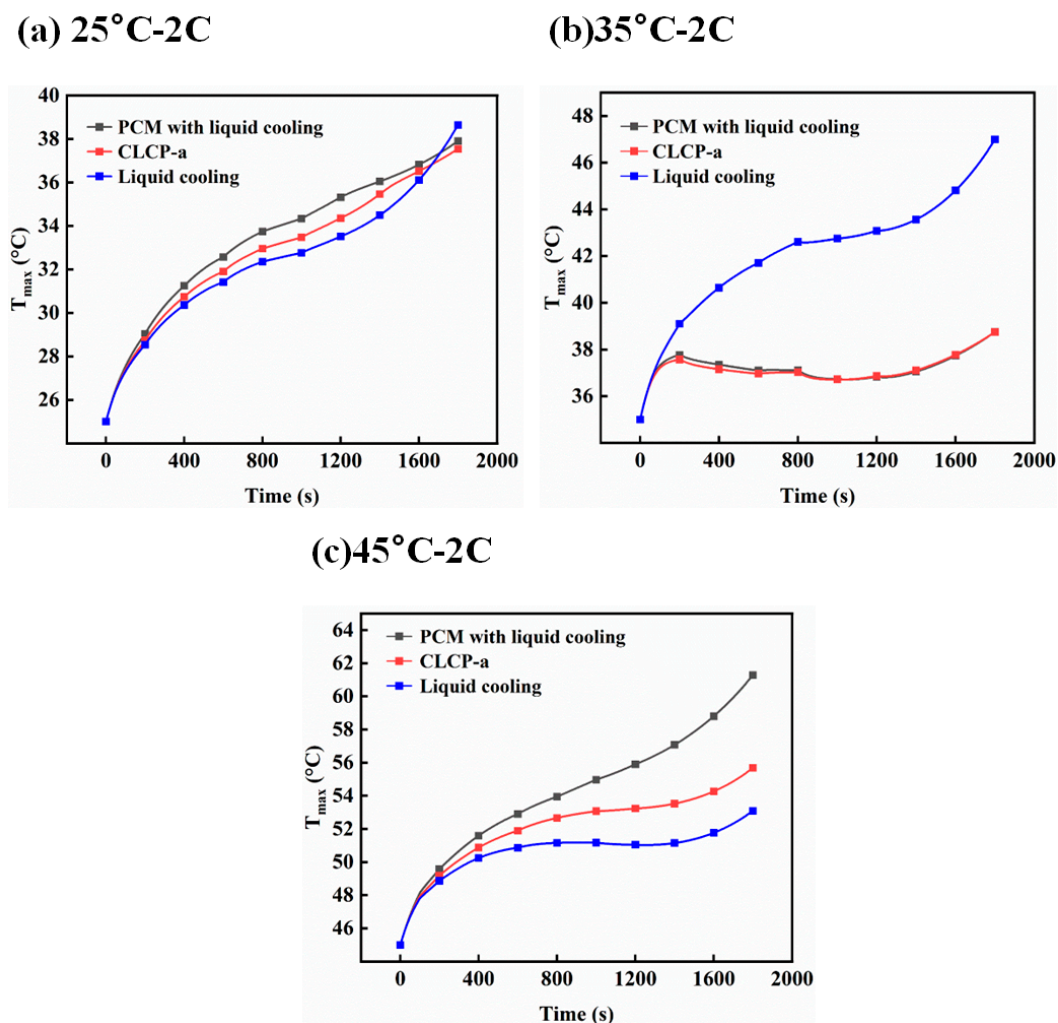


**Figure 9.** Temperature curves of three thermal management systems for (a) 25 °C—2 C, (b) 35 °C—2 C, and (c) 45 °C—2 C.

However, due to the low thermal conductivity of the PCM, when the temperature was too high and the PCM failed, the PCM could no longer control the temperature rise of the battery module but rather hindered the heat dissipation of the battery module. As shown in Figure 9c, the PCM failed and ensured that the heat inside the BTMS could not be taken away by liquid cooling in time. At approximately 800 s–1400 s, the liquid cooling could control the temperature of the battery module within a certain range and the temperature no longer rose, while the other groups could not effectively control the temperature and

it continued to rise. Not using PCM at this time could produce the best cooling effect. Although the PCM inside CLCP-a had failed, the battery module temperature rise curve was still flatter than those for the other two battery modules that used the PCM due to its aluminum heat-conducting shell.

The above results showed that when the PCM was in working condition, CLCP-a had a more comprehensive performance and could control the  $T_{\max}$  rise of the battery module to a certain extent even after the PCM failed.

### 3.2. Effect of Channel Shape

Five types of flow channels (Figure 3) were designed to evaluate their performance in the BTMS. The results are shown in Figure 10. As described in this section, the inlet temperature was set as 25 °C, and the flow velocity was set as 0.005 m/s. During the PCM working period, for which the ambient temperature was 25 °C or 35 °C, the five types of flow channels had little impact on the  $T_{\max}$  and  $\Delta T_{\max}$  due to the buffering effect of the PCM. Therefore, the  $T_{\max}$  of the battery could be controlled below 40 °C and the  $\Delta T_{\max}$  could be less than 5 °C, except for the b and c flow channels. For a 45 °C ambient temperature case, the PCM lost its effect, and all of the heat of the battery module was taken away by active liquid cooling. In addition, due to the poor thermal conductivity of the PCM, it was more difficult for the liquid cooling to dissipate heat. Therefore, it was particularly important that a reasonable flow channel design could effectively reduce the  $T_{\max}$  and  $\Delta T_{\max}$  of the battery module. As can be seen from Figure 10, the e-type flow channel was more effective in cooling and equalizing the temperature of the battery module than the other four types of flow channels, and it was shown that the  $T_{\max}$  was 4.2% lower and the  $\Delta T_{\max}$  was reduced by 32.8% compared to the other four types of flow channels. The e-type flow channel  $T_{\max}$  only increased by 21.7% when compared to the ambient temperature, which was the best flow channel.

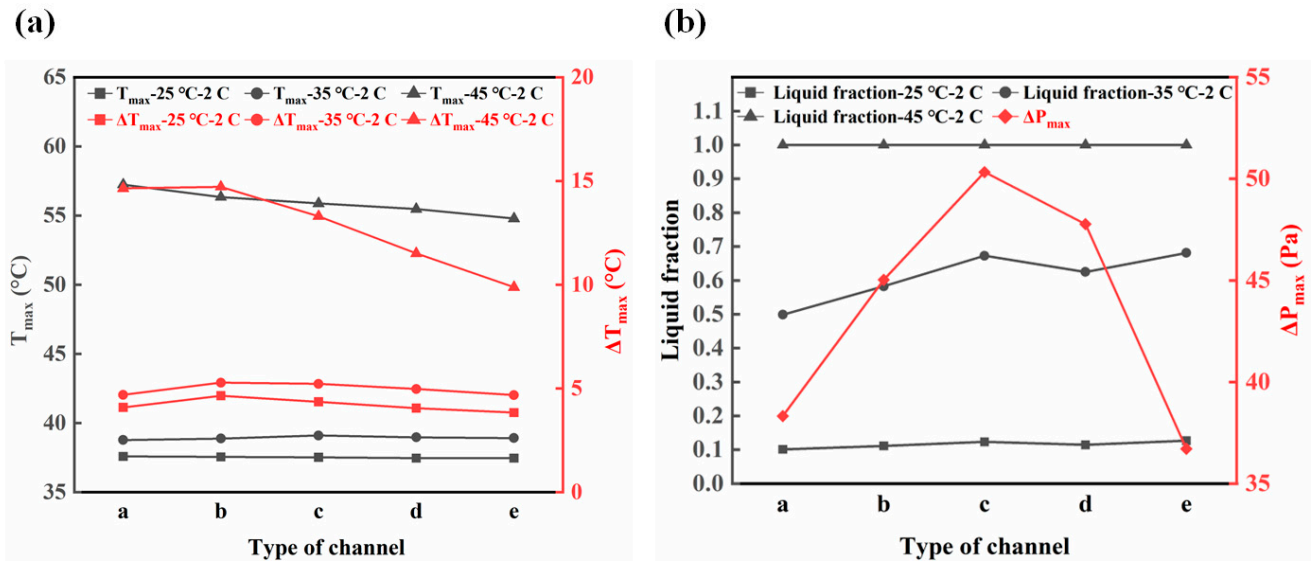


**Figure 10.** (a) Maximum temperature and maximum temperature difference, and (b) liquid fraction and maximum pressure drop for five channel configurations.

The e-type flow channel had the best comprehensive performance under the three working conditions. Further, the pressure drop was also the smallest. The pressure distribution cloud diagram is shown in Figure 11. Compared with the other four types of flow channels, the e-type flow channel first ran through the center of the battery module and then spread to the edges. The d-type flow channel had a similar design; that is, the center position with the highest temperature in the battery module had cooling priority, so the d-type flow channel and the e-type flow channel could have better cooling and temperature control performance. At the same time, the e-type flow channel had a higher

utilization rate of phase change materials. This might have been because more of the wall surface of the flow channel increased the heat transfer area between the battery and the PCM, ensuring that the heat could be better transferred to the PCM.

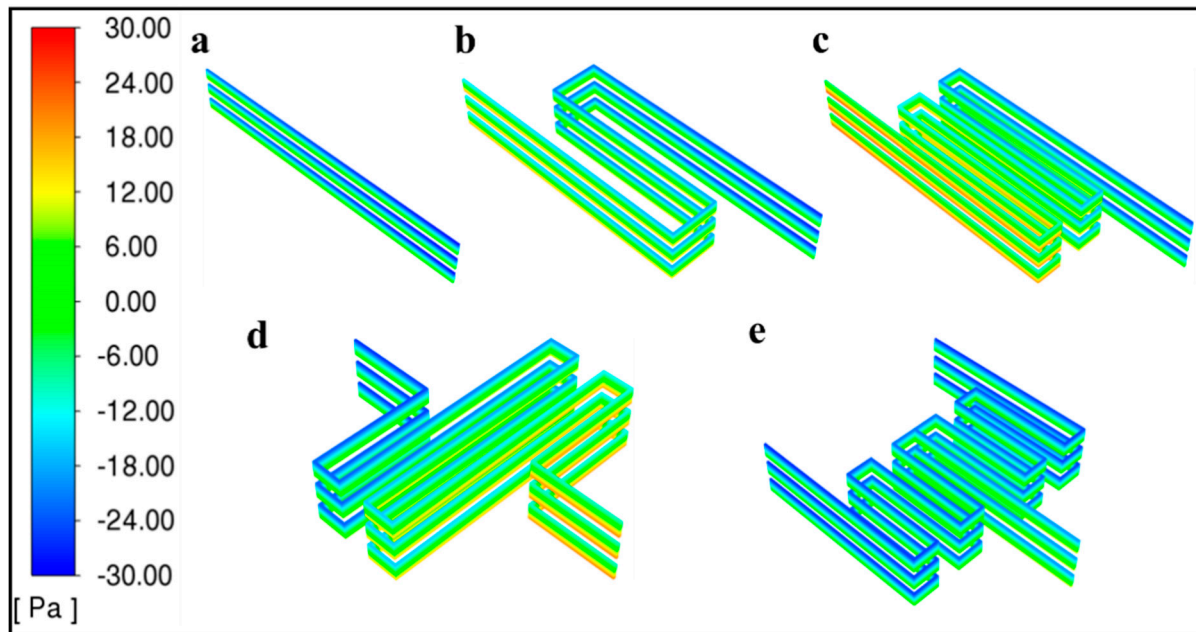


**Figure 11.** Pressure distribution diagrams of five flow channel configurations: (a) a-type flow channel, (b) b-type flow channel, (c) c-type flow channel, (d) d-type flow channel, and (e) e-type flow channel.

### 3.3. Effect of Inlet Temperature

As discussed in the previous section, by comparing the effects of different flow channels on the performance of the BTMS, it was determined that the e-type flow channel had the best overall performance. Therefore, in the subsequent discussion of the effects of different boundary conditions on the BTMS, the e-type flow channel was selected. In this subsection, the effect of the coolant inlet temperature on the BTMS is discussed.

As shown in Figure 12, for the ambient temperatures of 25 °C/35 °C/45 °C, the effects of the coolant inlet temperatures of 17–29 °C/27–39 °C/37–49 °C on the battery were discussed. It can be seen that at an ambient temperature of 25 °C (Figure 12a), the increase in the coolant inlet temperature could improve the temperature uniformity and the  $T_{\max}$  of the battery module, as well as the liquid fraction of the PCM. However, due to the effect of the PCM, changes in the coolant inlet temperature had little impact on the  $T_{\max}$ , and the  $\Delta T_{\max}$  was much more sensitive to changes in the inlet temperature. Therefore, the temperature uniformity was a matter of concern first, and a higher temperature in the range of 17–29 °C was chosen, which was equal to or slightly higher than the ambient temperature, which helped improve the temperature uniformity of the battery module. When the ambient temperature was 35 °C (Figure 12b), the increase in the inlet temperature first increased the temperature uniformity and then decreased the temperature uniformity when the inlet temperature was over 35 °C. When the inlet temperature was 35 °C, which was the ambient temperature, the battery module had the best temperature uniformity of 2.49 °C. However, when the inlet temperature was higher than 35 °C, the  $T_{\max}$  increased sharply instead of increasing gently. Thus, 35 °C was the best inlet temperature in this case. When the ambient temperature was 45 °C (Figure 12c), the PCM was in a liquid state at the beginning. By comparing the absolute values of the slopes of the  $T_{\max}$  and the  $\Delta T_{\max}$ , the factor that was more sensitive to the changes in the inlet temperature could be determined. The absolute value of the slope of the  $T_{\max}$  was 0.218, while the  $T_{\max}$  changed from 57.38 °C to 59.99 °C. Additionally, the absolute value of the slope of the  $\Delta T_{\max}$  was 0.259, while the  $\Delta T_{\max}$  changed from 6.75 °C to 3.63 °C. Hence, the  $\Delta T_{\max}$  was more sensitive than the  $T_{\max}$ .

for the changes in the inlet temperature. When the coolant inlet temperature was 45 °C, the  $\Delta T_{\max}$  of the battery module was less than 5 °C, so it was more appropriate to choose 45 °C as the inlet temperature.

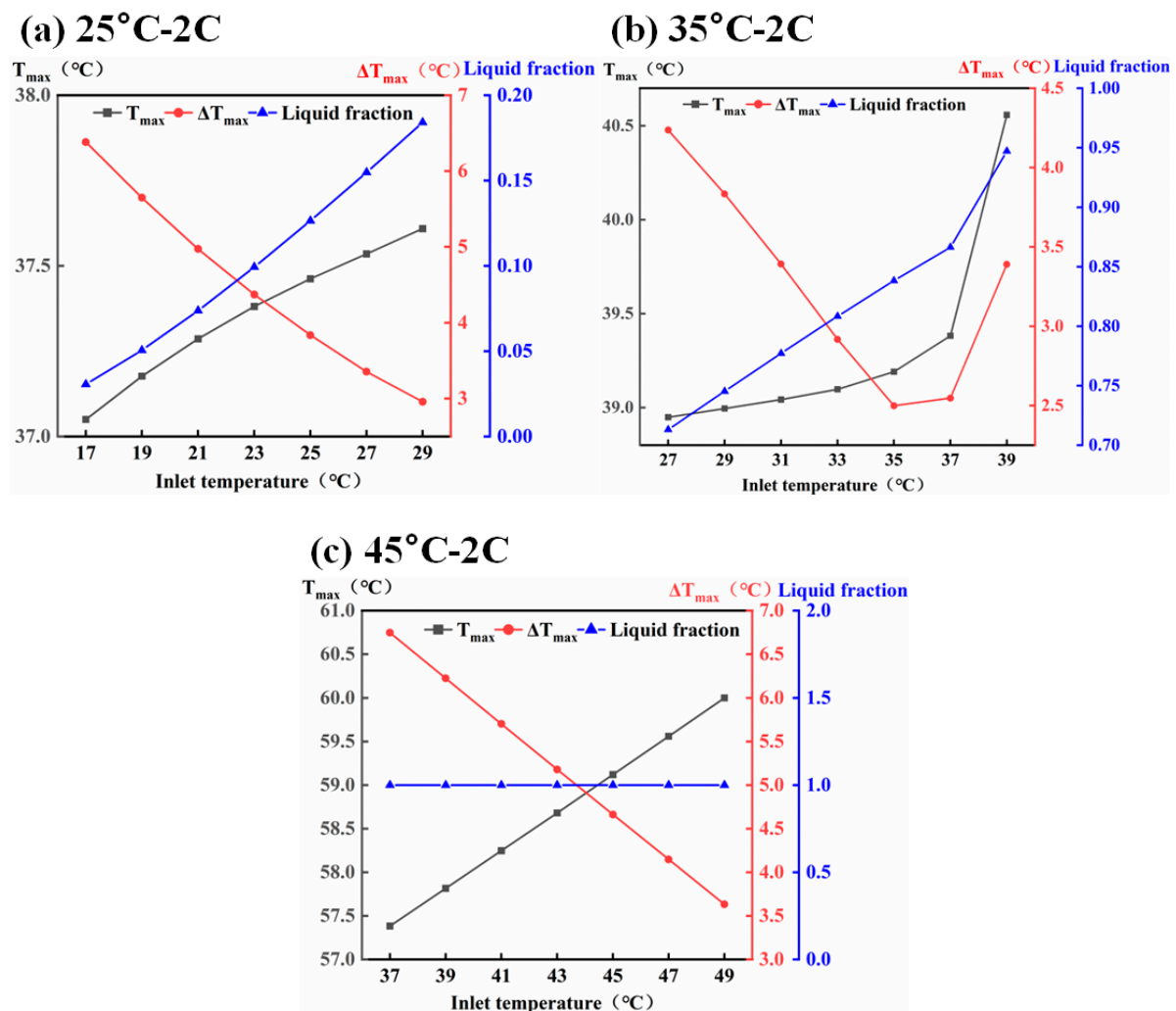


**Figure 12.** Performance comparison of different inlet temperatures for (a) 25 °C—2 C, (b) 35 °C—2 C, and (c) 45 °C—2 C operating conditions.

There is no doubt that increasing the inlet temperature will also increase the  $T_{\max}$  of a battery module and the liquid fraction of a PCM. Although reaching a higher  $T_{\max}$  is not the BTMS's expected function, it may also be helpful in some specific situations. For example, a higher inlet temperature helps to increase the temperature of the phase change material, which allows the material to reach the phase change temperature and enter the working state as soon as possible. Further, due to the effect of the latent heat, the maximum temperature of the battery module is not sensitive to changes in the inlet temperature, so this can improve the temperature uniformity greatly, while the maximum temperature only has a slight increase. However, increasing the inlet temperature will not always improve the temperature uniformity of a battery module. When the inlet temperature is higher than or close to the maximum temperature of the battery module during discharge, the coolant will become a heat source for the battery. This severely deteriorates the  $T_{\max}$  and  $\Delta T_{\max}$  of the battery module. Therefore, it may be a more appropriate choice to select a temperature that is equal to or slightly higher than the ambient temperature as the coolant inlet temperature.

### 3.4. Effect of Inlet Velocity

In this section, the impact of the coolant inlet velocity on the performance of the battery thermal management system while using 25 °C as the inlet temperature is discussed, as shown in Figure 13. It can be seen that an increase in the inlet velocity reduced the  $T_{\max}$  of the battery and the liquid fraction of PCM in the above three cases. This showed that the BTMS became more reliant on the active liquid cooling to take out the heat as the inlet velocity increased. However, the passive PCM cooling was inhibited by the excessive inlet velocity of the active liquid cooling. As shown in Figure 13a, when the inlet velocity was 0.015 m/s, the liquid fraction of the PCM in the BTMS at the 25 °C ambient temperature was close to zero. Continuing to increase the inlet flow rate would lead to the maximum temperature of the battery module decreasing sharply and the  $\Delta T_{\max}$  of the battery module exceeding 5 °C. When the flow rate continued to increase, due to the  $T_{\max}$  of the battery module decreasing sharply, the temperature difference between the battery and coolant also decreased, which led to the  $\Delta T_{\max}$  of the battery module being reduced. The same situation also occurred under the ambient temperature condition of 45 °C (Figure 13b).

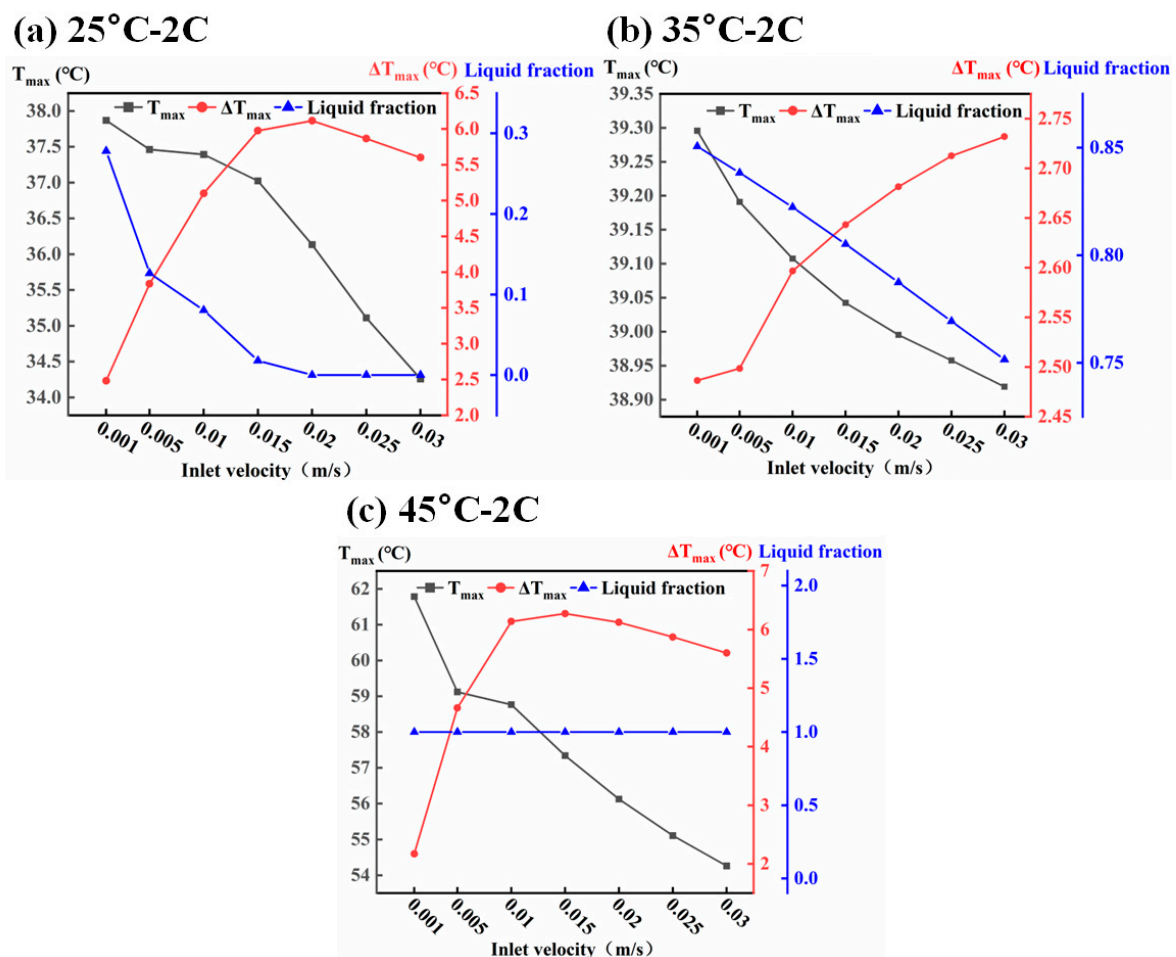


**Figure 13.** Performance comparison of different inlet velocities for (a) 25 °C—2 C, (b) 35 °C—2 C, and (c) 45 °C—2 C operating conditions.

Nevertheless, under the condition of a 35 °C ambient temperature (Figure 13c), the relationship between the  $\Delta T_{\max}$  of the battery module and the coolant inlet flow rate did not show the abovementioned trend. The  $T_{\max}$  and  $\Delta T_{\max}$  of the battery module did not change drastically with the change in the inlet velocity. When the inlet velocity increased from 0.001 m/s to 0.03 m/s, the  $T_{\max}$  only decreased by 0.38 °C, and the  $\Delta T_{\max}$  only increased by 0.25 °C. During this process, the liquid fraction was always maintained at a high value. It

could be speculated that when liquid cooling served as the main cooling method, that is, when the PCM was suppressed or failed, the various thermal performances of the battery module changed drastically when the coolant inlet flow rate changed. Therefore, the higher inlet velocity did not always lead to a better thermal performance. When the working conditions between PCM cooling and liquid cooling were in a relative balance, the thermal indicators of the battery module did not change drastically with the change in the inlet velocity, which illustrated that the PCM had a certain thermal buffering effect on the battery module. For this BTMS, the high inlet velocity did not produce a better thermal performance. In contrast, a high inlet velocity would inhibit the effect of the PCM in this BTMS. Further, the high inlet velocity also added additional power consumption. Thus, 0.001 m/s or 0.005 m/s was a relatively reasonable inlet velocity for this BTMS.

### 3.5. Effect of Reverse Flow

This section describes how three different reverse flow modes were designed for the hybrid BTMS in this research, as shown in Figure 14. The thermal performance of the system was compared under the ambient temperature condition of 45 °C. The inlet flow velocity was 0.005 m/s and the inlet temperature was 45 °C. The results are shown in Figure 15.

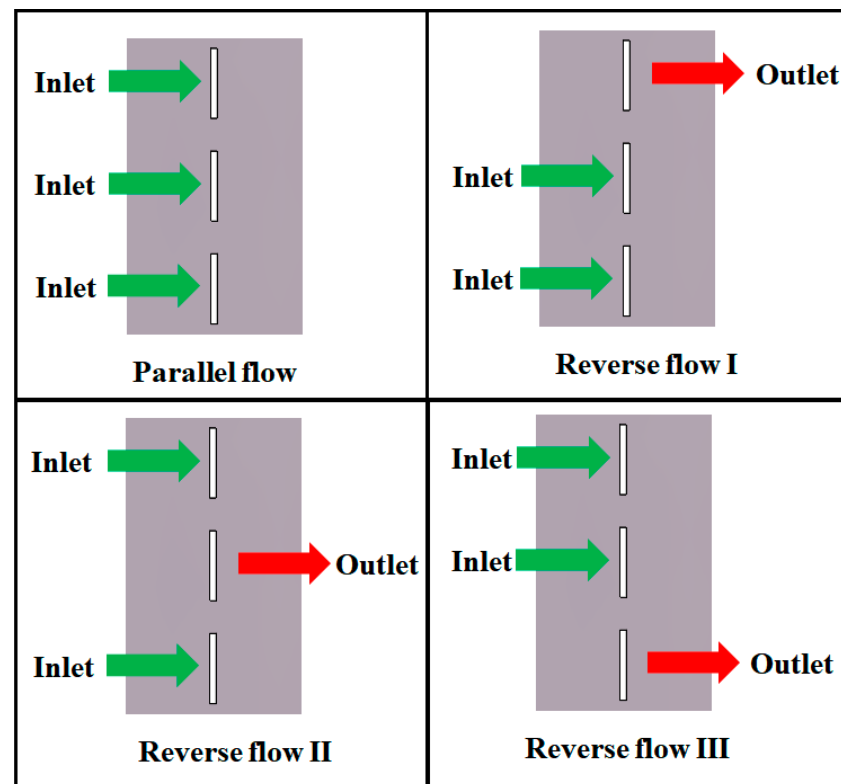


Figure 14. Diagram of four flow settings' design.

Three reverse flow methods could effectively reduce the  $T_{\max}$  and  $\Delta T_{\max}$  of the battery module. With the decrease in the  $T_{\max}$ , reverse flow I and reverse flow III worked more effectively. The  $T_{\max}$  was 29.9% higher than the ambient temperature, while reverse flow II was 30.0% higher than the ambient temperature. However, reverse flow II was much more effective in improving the temperature uniformity, and the  $\Delta T_{\max}$  was 35.7% lower than the parallel flow, while reverse flow I and reverse flow III were only 29.9% lower than the parallel flow. This showed that using reverse flow could effectively improve the  $\Delta T_{\max}$  of the battery module, and also had a slight effect on reducing the maximum temperature of

the battery module. Overall, among the three reverse flow methods designed, reverse flow II could achieve the best overall result.

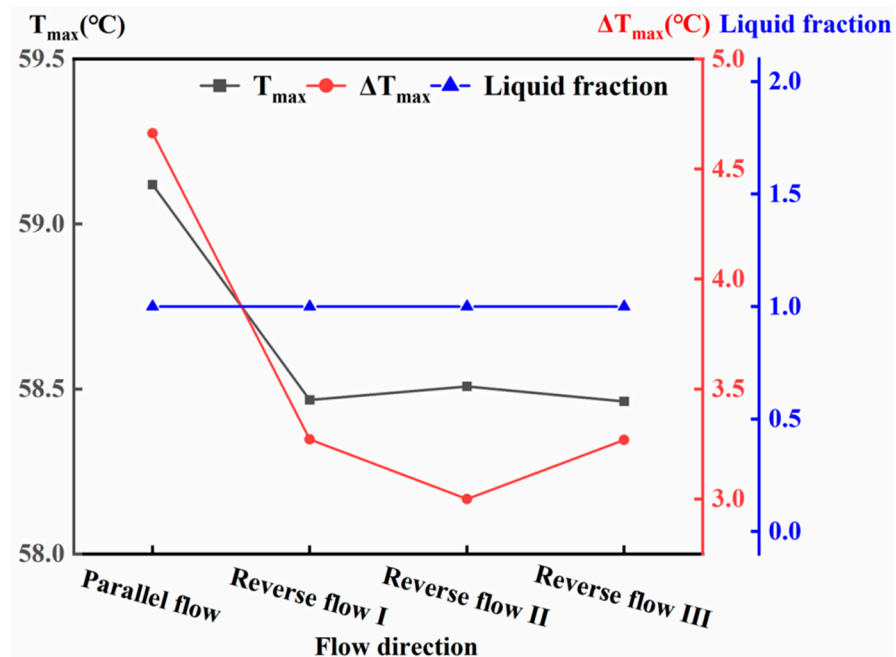


Figure 15. Performance variations of four flow settings under 45 °C—2 C operating conditions.

## 4. Conclusions and Research Recommendations

### 4.1. Conclusions

In this work, a novel BTMS was designed for an 18,650 cylindrical battery module, which was equipped with PCM inside and an athermal conduction slot that fitted the battery, forming a creative hybrid PCM/liquid-cooling system. The effectiveness of this system was verified by comparing traditional thermal management systems, such as liquid cooling and traditionally designed PCM-coupled liquid cooling. Based on this, the influences of the flow channel configurations, coolant inlet temperature, coolant inlet flow rate, and reverse flow on the thermal performance of the system were discussed in detail. The main conclusions could be drawn as follows:

(1) The proposed BTMS with the newly designed PCM composite liquid-cooling heat dissipation model demonstrated the optimum thermal management effect compared to that of pure PCM cooling, liquid cooling, and conventionally designed PCM composite liquid cooling. The weight of the same volume was reduced by 50.2% when compared to liquid cooling. Under 35 °C—2 C operating conditions, the aforementioned BTMS could reduce the  $T_{max}$  by 17.5% and the  $\Delta T_{max}$  by 19.5% compared to liquid cooling. Compared with conventionally designed PCM composite liquid cooling, the maximum temperature difference was reduced by 34.9%.

(2) By optimizing the flow channel configuration, the preferential cooling of the center of the battery module could provide better temperature uniformity. When the flow channel traversed the battery as much as possible, the flow channel wall could provide more highly thermally conductive interfaces between the battery and the PCM, thereby improving the utilization of the PCM. Under the working condition of 45 °C—2 C, the  $T_{max}$  of the e-type flow channel only increased by 21.7% when compared with the ambient temperature, and the  $\Delta T_{max}$  was reduced by 32.5% when compared to the parallel flow.

(3) It could be found that when the PCM was in the working state, different factors had a small impact on the thermal performance of the system. In contrast, when the PCM failed, the impact was greater. This fully demonstrated that the PCM had a buffering effect on the system. When the PCM fails, the consideration of the latent heat recovery might lead to a better thermal performance.

(4) A reasonable inlet flow rate and inlet temperature helped balance the interaction between the PCM and liquid cooling and reduced system power consumption. When the PCM had not yet reached the melting temperature, a slightly higher inlet temperature could be used to make the PCM melt in advance. For the working condition of 35 °C—2 C, when 35 °C was selected as the inlet temperature, the maximum decrease in the  $\Delta T_{\max}$  was 40.9%. Additionally, the minimum increase in the  $T_{\max}$  was 11.9% when compared to the ambient temperature. Under the working condition of 45 °C—2 C, when 0.001 m/s was selected as the inlet velocity, the maximum drop in the  $\Delta T_{\max}$  was 65.4%.

(5) Reverse flow could effectively reduce the  $\Delta T_{\max}$  of the battery module and reduce the  $T_{\max}$  of the battery module. Compared with the ambient temperature, the minimum increase in the  $T_{\max}$  occurred when using reverse flow I and reverse flow III, which were both 21.7%. Compared with the parallel flow case, the largest drop in  $\Delta T_{\max}$  occurred when using reverse flow II, which was 35.7%.

#### 4.2. Research Recommendations

The effect of the proposed new leak-proof with thermal conduction slot PCM-coupled BTMS was simulated and analyzed in this research, and the effectiveness and advancement of this system were verified. However, there is still related work that requires further research on this topic. Specific suggestions are as follows:

(1) This research did not involve the simulation of the electrochemical performance but only simulated the temperature performance. Subsequent work will supplement the simulation research on the electrochemical performance of a battery.

(2) Here, by comparing the working conditions under three working conditions, it was concluded that whether or not the PCM was in working condition had a huge impact on the thermal performance of the system, but the latent heat recovery of the phase change material was not discussed. This will be supplemented in subsequent work.

(3) The battery working state simulated in this research was only the discharge state, without containing the entire battery charging/discharging process or the cycle. In subsequent work, the performance of the BTMS for the battery charging/discharging cycle will be supplemented and calculated.

**Author Contributions:** Conceptualization, J.Z.; Writing—original draft preparation, W.Z.; Writing—review and editing, Y.H.; Supervision, J.Z.; Funding acquisition, J.Z., G.Z. and Y.H.; Resources, G.Z., D.S., L.J. and Y.W. All authors have read and agreed to the published version of the manuscript.

**Funding:** This work was supported by Science and Technology Program of Guangzhou, China (202201011357), Science and Technology Project of Guangdong Administration for Market Regulation (2023ZZ06), the National Natural Science Foundation of China (52006040), Zhuhai Science and Technology Planning Project in the Field of Social Development (2220004000343, ZH22036201210039PWC), Guangzhou Science and Technology Plan Project (202201010226, 202201010050). All authors have confirmed the funding information.

**Data Availability Statement:** Data is contained within the article.

**Conflicts of Interest:** Author Yuliang Wen was employed by the Dongguan Guixiang Insulation Material Co., Ltd. The remaining authors declare that the research was conducted in the absence of any commercial or financial relationships that could be construed as a potential conflict of interest.

#### Nomenclature

EVs	Electric vehicles	I	Current
BTMS	Battery thermal management system	N	Number of charges associated with the reaction
PCM	Phase change material	F	Faraday's constant
CPCM	Composite phase change material	$R_p$	Battery polarization resistance
HPCM	High-thermal-conductivity material	$R_e$	Battery internal resistance
LPCM	Low-thermal-conductivity material	$R_t$	Battery total resistance

PA	Paraffin	$q$	Battery heat generation
EKF	Extended Kalman filter	$V$	Volume of battery
TR	Thermal runaway	$E_{OC}$	Balance electromotive force of battery
CFD	Computational fluid dynamics	$U$	Operating potential of battery
CLCP	Composite liquid-cooling plate	$T$	Operating temperature of battery
DOD	Depth of discharge	$Re$	Reynolds number
EG	Expanded graphite	$\rho_c$	Density of coolant
$T_{max}$	Maximum temperature	$v_c$	Velocity of coolant
$\Delta T_{max}$	Maximum temperature difference	$d_c$	Hydraulic diameter of channel
$Q_{gen}$	Total heat generated by battery	$P_c$	Wetted perimeter of flow channel
$Q_r$	Battery reaction heat	$\rho_b$	Density of battery
$Q_p$	Battery polarization heat	$\rho_{PCM}$	Density of PCM
$Q_j$	Battery joule heat	$k_{PCM}$	Thermal conductivity of PCM
$T_b$	Temperature of the battery	$T_0$	Ambient temperature
$A_c$	Cross-sectional area of flow channel	$T_s$	Solid phase temperatures of PCM
$r_c$	Radius of flow channel	$\rho_c$	Density of coolant
$k_b$	Thermal conductivity of battery	$C_{p,c}$	Specific heat capacity of coolant
$H_{pcm}$	Enthalpy of PCM	$k_c$	Thermal conductivity of coolant
$T_{PCM}$	Temperature of PCM	$T_c$	Temperature of coolant
$\beta$	Liquid fraction of PCM	$\vec{v}_c$	Coolant velocity vector
$T_l$	Liquid phase temperatures of PCM	$\mu_c$	Coolant dynamic viscosity
$\rho_t$	Density of flow channel	$\frac{\partial T}{\partial n}$	Temperature gradient
$C_{p,t}$	Specific heat capacity of flow channel	$T_{tube}$	Surface temperature of internal channel
$k_t$	Thermal conductivity of flow channel	$k_{plate}$	Thermal conductivity of liquid-cooling plate
$T_t$	Temperature of flow channel	$h_c$	Heat transfer coefficient of liquid coolant
$P$	Coolant static pressure	$h$	Natural convection heat transfer coefficient

## References

- Cai, S.; Zhang, X.; Ji, J. Recent advances in phase change materials-based battery thermal management systems for electric vehicles. *J. Energy Storage* **2023**, *72*, 108750. [\[CrossRef\]](#)
- Lin, J.; Liu, X.; Li, S.; Zhang, C.; Yang, S. A review on recent progress, challenges and perspective of battery thermal management system. *Int. J. Heat Mass Transf.* **2021**, *167*, 120834. [\[CrossRef\]](#)
- Zhang, W.; Zhang, J.; Hu, Y.; Zhang, L.; Zhang, W.; Chen, Y.; Zhang, G.; Jiang, L.; Dai, Z.; Wen, Y. Investigations on the essential causes of the degrading properties of ternary lithium-ion batteries with different nickel content during thermal runaway stage. *Int. J. Electrochem. Sci.* **2024**, *19*, 100491. [\[CrossRef\]](#)
- Xu, B.; Lee, J.; Kwon, D.; Kong, L.X.; Pecht, M. Mitigation strategies for Li-ion battery thermal runaway: A review. *Renew. Sustain. Energy Rev.* **2021**, *150*, 111437. [\[CrossRef\]](#)
- Shahjalal, M.; Shams, T.; Islam, M.E.; Alam, W.; Modak, M.; Hossain, S.B.; Ramadesigan, V.; Ahmed, M.R.; Ahmed, H.; Iqbal, A. A review of thermal management for Li-ion batteries: Prospects, challenges, and issues. *J. Energy Storage* **2021**, *39*, 102518. [\[CrossRef\]](#)
- Dan, D.; Zhao, Y.; Wei, M.; Wang, X. Review of Thermal Management Technology for Electric Vehicles. *Energies* **2023**, *16*, 4693. [\[CrossRef\]](#)
- Chavan, S.; Venkateswarlu, B.; Prabakaran, R.; Salman, M.; Joo, S.W.; Choi, G.S.; Kim, S.C. Thermal runaway and mitigation strategies for electric vehicle lithium-ion batteries using battery cooling approach: A review of the current status and challenges. *J. Energy Storage* **2023**, *72*, 108569. [\[CrossRef\]](#)
- Yang, Q.; Xu, C.; Geng, M.; Meng, H. A review on models to prevent and control lithium-ion battery failures: From diagnostic and prognostic modeling to systematic risk analysis. *J. Energy Storage* **2023**, *74*, 109230. [\[CrossRef\]](#)
- Zhang, X.; Li, Z.; Luo, L.; Fan, Y.; Du, Z. A review on thermal management of lithium-ion batteries for electric vehicles. *Energy* **2022**, *238*, 121652. [\[CrossRef\]](#)
- Luo, J.; Zou, D.; Wang, Y.; Wang, S.; Huang, L. Battery thermal management systems (BTMs) based on phase change material (PCM): A comprehensive review. *Chem. Eng. J.* **2022**, *430*, 132741. [\[CrossRef\]](#)
- Jaguemont, J.; Bardé, F. A critical review of lithium-ion battery safety testing and standards. *Appl. Therm. Eng.* **2023**, *231*, 121014. [\[CrossRef\]](#)
- Kumar, R.; Goel, V. A study on thermal management system of lithium-ion batteries for electrical vehicles: A critical review. *J. Energy Storage* **2023**, *71*, 108025. [\[CrossRef\]](#)
- Thakur, A.K.; Sathyamurthy, R.; Velraj, R.; Saidur, R.; Pandey, A.; Ma, Z.; Singh, P.; Hazra, S.K.; Sharshir, S.W.; Prabakaran, R. A state-of-the art review on advancing battery thermal management systems for fast-charging. *Appl. Therm. Eng.* **2023**, *226*, 120303. [\[CrossRef\]](#)

14. Detka, K.; Górecki, K. Selected Technologies of Electrochemical Energy Storage—A Review. *Energies* **2023**, *16*, 5034. [[CrossRef](#)]
15. Maiorino, A.; Cilenti, C.; Petruzzello, F.; Aprea, C. A review on thermal management of battery packs for electric vehicles. *Appl. Therm. Eng.* **2023**, *238*, 122035. [[CrossRef](#)]
16. Li, W.; Zhou, Y.; Zhang, H.; Tang, X. A Review on Battery Thermal Management for New Energy Vehicles. *Energies* **2023**, *16*, 4845. [[CrossRef](#)]
17. Shen, Z.-G.; Chen, S.; Liu, X.; Chen, B. A review on thermal management performance enhancement of phase change materials for vehicle lithium-ion batteries. *Renew. Sustain. Energy Rev.* **2021**, *148*, 111301. [[CrossRef](#)]
18. Anisha; Kumar, A. Identification and Mitigation of Shortcomings in Direct and Indirect Liquid Cooling-Based Battery Thermal Management System. *Energies* **2023**, *16*, 3857. [[CrossRef](#)]
19. Tete, P.R.; Gupta, M.M.; Joshi, S.S. Developments in battery thermal management systems for electric vehicles: A technical review. *J. Energy Storage* **2021**, *35*, 102255. [[CrossRef](#)]
20. Khan, M.M.; Alkhedher, M.; Ramadan, M.; Ghazal, M. Hybrid PCM-based thermal management for lithium-ion batteries: Trends and challenges. *J. Energy Storage* **2023**, *73*, 108775. [[CrossRef](#)]
21. Akkurt, N.; Aghakhani, S.; Mahmoud, M.Z.; Tag El Din, E.M. The influence of battery distance on a hybrid air-cooled cylindrical lithium-ion battery phase change material thermal management system for storing solar energy. *J. Energy Storage* **2022**, *52*, 104873. [[CrossRef](#)]
22. Shengxin, E.; Liu, Y.; Cui, Y.; Wu, A.; Yin, H. Effects of composite cooling strategy including phase change material and cooling air on the heat dissipation performance improvement of lithium ion power batteries pack in hot climate and its catastrophe evaluation. *Energy* **2023**, *283*, 129074.
23. Liu, Z.; Huang, J.; Cao, M.; Jiang, G.; Yan, Q.; Hu, J. Experimental study on the thermal management of batteries based on the coupling of composite phase change materials and liquid cooling. *Appl. Therm. Eng.* **2021**, *185*, 116415. [[CrossRef](#)]
24. Hekmat, S.; Bamdezh, M.A.; Molaieimesh, G.R. Hybrid thermal management for achieving extremely uniform temperature distribution in a lithium battery module with phase change material and liquid cooling channels. *J. Energy Storage* **2022**, *50*, 104272. [[CrossRef](#)]
25. Xin, Q.Q.; Yang, T.Q.; Zhang, H.Y.; Yang, J.X.; Zeng, J.; Xiao, J.S. Experimental and numerical study of lithium-ion battery thermal management system using composite phase change material and liquid cooling. *J. Energy Storage* **2023**, *71*, 108003. [[CrossRef](#)]
26. Zhao, Y.; Zhang, X.; Yang, B.; Cai, S. A review of battery thermal management systems using liquid cooling and PCM. *J. Energy Storage* **2024**, *76*, 109836. [[CrossRef](#)]
27. Bernagozzi, M.; Georgoulas, A.; Miche, N.; Marengo, M. Heat pipes in battery thermal management systems for electric vehicles: A critical review. *Appl. Therm. Eng. Des. Process. Equip. Econ.* **2023**, *219*, 119495. [[CrossRef](#)]
28. Fathoni, A.M.; Putra, N.; Mahlia, T.I. A systematic review of battery thermal management systems based on heat pipes. *J. Energy Storage* **2023**, *73*, 109081. [[CrossRef](#)]
29. Li, Q.; Cho, J.-R.; Zhai, J. Optimization of Thermal Management System with Water and Phase Change Material Cooling for Li-Ion Battery Pack. *Energies* **2021**, *14*, 5312. [[CrossRef](#)]
30. Liu, H.; Ahmad, S.; Shi, Y.; Zhao, J. A parametric study of a hybrid battery thermal management system that couples PCM/copper foam composite with helical liquid channel cooling. *Energy* **2021**, *231*, 120869. [[CrossRef](#)]
31. Zhang, W.C.; Liang, Z.C.; Yin, X.X.; Ling, G.Z. Avoiding thermal runaway propagation of lithium-ion battery modules by using hybrid phase change material and liquid cooling. *Appl. Therm. Eng.* **2021**, *184*, 116380. [[CrossRef](#)]
32. Cao, J.; Ling, Z.; Fang, X.; Zhang, Z. Delayed liquid cooling strategy with phase change material to achieve high temperature uniformity of Li-ion battery under high-rate discharge. *J. Power Sources* **2020**, *450*, 227673. [[CrossRef](#)]
33. Liu, Z.; Xu, G.; Xia, Y.; Tian, S. Numerical study of thermal management of pouch lithium-ion battery based on composite liquid-cooled phase change materials with honeycomb structure. *J. Energy Storage* **2023**, *70*, 108001. [[CrossRef](#)]
34. Xiao, J.; Zhang, X.; Bénard, P.; Yang, T.; Zeng, J.; Long, X. Fin structure and liquid cooling to enhance heat transfer of composite phase change materials in battery thermal management system. *Energy Storage* **2023**, *5*, e453. [[CrossRef](#)]
35. Javani, N.; Dincer, I.; Naterer, G.; Yilbas, B. Exergy analysis and optimization of a thermal management system with phase change material for hybrid electric vehicles. *Appl. Therm. Eng.* **2014**, *64*, 471–482. [[CrossRef](#)]
36. Zhao, Y.; Li, Q.; Zou, B.; Zhang, T.; Jin, L.; Qiao, G.; Nie, B.; Huang, Y.; Ding, Y. Performance of a liquid cooling-based battery thermal management system with a composite phase change material. *Int. J. Energy Res.* **2020**, *44*, 4727–4742. [[CrossRef](#)]
37. Zhang, W.; Huang, L.; Zhang, Z.; Li, X.; Ma, R.; Ren, Y.; Wu, W. Non-uniform phase change material strategy for directional mitigation of battery thermal runaway propagation. *Renew. Energy* **2022**, *200*, 1338–1351. [[CrossRef](#)]
38. Ouyang, T.; Liu, B.; Xu, P.; Wang, C.; Ye, J. Electrochemical-thermal coupled modelling and multi-measure prevention strategy for Li-ion battery thermal runaway. *Int. J. Heat Mass Transf.* **2022**, *194*, 123082. [[CrossRef](#)]
39. Chen, X.; Zhou, F.; Yang, W.; Gui, Y.; Zhang, Y. A hybrid thermal management system with liquid cooling and composite phase change materials containing various expanded graphite contents for cylindrical lithium-ion batteries. *Appl. Therm. Eng.* **2022**, *200*, 117702. [[CrossRef](#)]
40. Zhang, Y.; Fu, Q.; Liu, Y.; Lai, B.; Ke, Z.; Wu, W. Investigations of Lithium-Ion Battery Thermal Management System with Hybrid PCM/Liquid Cooling Plate. *Processes* **2022**, *11*, 57. [[CrossRef](#)]

41. Lebrouhi, B.E.; Lamrani, B.; Ouassaid, M.; Abd-Lefdil, M.; Maaroufi, M.; Kousksou, T. Low-cost numerical lumped modelling of lithium-ion battery pack with phase change material and liquid cooling thermal management system. *J. Energy Storage* **2022**, *54*, 105293. [[CrossRef](#)]
42. An, Z.; Luo, Y.; Zhang, C.; Li, D. Performance of chocolate bar-shaped modular thermal management system combined metal lattice liquid-cooling plate with paraffin in high-rate discharge. *J. Energy Storage* **2022**, *56*, 106017. [[CrossRef](#)]
43. Hu, S.; Wang, S.; Ma, C.; Li, S.; Liu, X.; Zhang, Y. A hybrid cooling method with low energy consumption for lithium-ion battery under extreme conditions. *Energy Convers. Manag.* **2022**, *266*, 115831. [[CrossRef](#)]
44. Hou, G.; Liu, X.; He, W.; Wang, C.; Zhang, J.; Zeng, X.; Li, Z.; Shao, D. An equivalent circuit model for battery thermal management system using phase change material and liquid cooling coupling. *J. Energy Storage* **2022**, *55*, 105834. [[CrossRef](#)]
45. Xu, X.; Tong, G.; Li, R. Numerical study and optimizing on cold plate splitter for lithium battery thermal management system. *Appl. Therm. Eng.* **2020**, *167*, 114787. [[CrossRef](#)]
46. Bernardi, D.; Pawlikowski, E.; Newman, J. A general energy balance for battery systems. *J. Electrochem. Soc.* **1985**, *132*, 5. [[CrossRef](#)]
47. Kong, D.; Peng, R.; Ping, P.; Du, J.; Chen, G.; Wen, J. A novel battery thermal management system coupling with PCM and optimized controllable liquid cooling for different ambient temperatures. *Energy Convers. Manag.* **2020**, *204*, 112280. [[CrossRef](#)]
48. Amallesh, T.; Narasimhan, N.L. Introducing new designs of minichannel cold plates for the cooling of Lithium-ion batteries. *J. Power Sources* **2020**, *479*, 228775. [[CrossRef](#)]
49. Wang, H.T.; Tao, T.; Xu, J.; Mei, X.S.; Liu, X.Y.; Gou, P. Cooling capacity of a novel modular liquid-cooled battery thermal management system for cylindrical lithium ion batteries. *Appl. Therm. Eng.* **2020**, *178*, 115591. [[CrossRef](#)]
50. Xie, J.; Mo, C.; Zhang, G.; Yang, X. Thermal performance analysis of liquid cooling system with hierarchically thermal conductive skeleton for large-scaled cylindrical battery module in harsh working conditions. *Int. J. Heat Mass Transf.* **2023**, *215*, 124487. [[CrossRef](#)]

**Disclaimer/Publisher’s Note:** The statements, opinions and data contained in all publications are solely those of the individual author(s) and contributor(s) and not of MDPI and/or the editor(s). MDPI and/or the editor(s) disclaim responsibility for any injury to people or property resulting from any ideas, methods, instructions or products referred to in the content.